214 Vol. 41, No. 2 / February 2024 / Journal of the Optical Society of America A Research Article

Journal of the Optical Society of America A

OPTICS, IMAGE SCIENCE, AND VISION

# Experiment and theory of the complex refractive index of dense colloidal media

PETER N. A. SPEETS AND JEROEN KALKMAN*

*Department of Imaging Physics, Delft University of Technology, Lorentzweg 1, 2628 CJ, Delft, The Netherlands*
**j.kalkman@tudelft.nl*

*Received 27 October 2023; revised 12 December 2023; accepted 15 December 2023; posted 15 December 2023; published 12 January 2024*

**The complex refractive index is analyzed by measuring its scattering attenuation $\mu_s$, group index $n_g$, and group velocity dispersion (GVD) for 100 nm diameter silica nanoparticles dispersed in water. The experiments were performed for wavelengths between 410 nm and 930 nm. The experimental results were compared with different mixing models for the complex refractive index of colloidal suspensions. The group index linearly scaled with the volume fraction both in experiment and for all tested models. It was found that the GVD has a nonlinear dependence on volume fraction in agreement with the coupled dipole model of Parola *et al.* [J. Chem. Phys. 141, 124902 (2014)] The scattering attenuation is in good agreement with both the coupled dipole model and the low frequency quasi-crystalline approximation [J. Electromagn. Waves Appl. 2, 757 (1988)] that take particle correlations into account. With an iterative fitting procedure of all the data based on both the coupled dipole model and the quasi-crystalline approximation, the refractive index, porosity, and size of the nanoparticles were determined. We determined that the coupled dipole model is in best agreement with the data.** 

https://doi.org/10.1364/JOSAA.510603

## 1. INTRODUCTION

An important parameter describing electromagnetic wave propagation in optical materials is the complex refractive index. The real part of the refractive index is related to refraction, phase delay, and phase velocity of the wave. The imaginary part of the refractive index is related to the optical attenuation of the wave caused by scattering and absorption.

For optical materials composed of atomic or molecular mixtures the real part of the refractive index is well described by the Lorentz-Lorenz equation [1,2], which is based on the intrinsic polarizability of the atoms or molecules in the mixture. Colloidal media are composed of liquid or solid particles with a size range of 1–1000 nm in a molecular solvent. In a dilute colloidal suspension the real part of the refractive index is well approximated with the simple Arago-Biot mixing formula [3,4]. This describes the refractive index as the average refractive index of the host medium and the suspended particles, weighted by their volume fraction.

The first theoretical description of the effect of small particles on the real part of the effective refractive index was given by Garnett who used the Clausius-Mossotti relation to incorporate the effect of embedded gold and silver particles to describe the optical properties of colored glass [5]. Since then, various mixing models [6–25] have been derived for the effective refractive index of particulate media. With some exceptions [8,9,14], these models predict both the real part and the imaginary part of the effective refractive index. In many cases, the scattering models were developed to describe the attenuation, caused by absorption or scattering, but some obtained the refractive properties from the electric permittivity [8,14,21].

The full complex refractive index of a dilute particle suspension is well approximated with the simple and widely used mixing formula given by van de Hulst [16]. This model predicts both the real and imaginary parts of the effective refractive index from a given complex scattering amplitude, for example, from Mie theory. A disadvantage of the van de Hulst refractive index model is that it does not incorporate volume fraction dependent scattering. In other words, it does not take into account the correlations between the particle positions and predicts a linear relationship between the effective refractive index and the volume fraction. The van de Hulst refractive index is applicable for volume fractions lower than 1% [22], but for higher volume fractions leads to erroneous results as the relationship between the imaginary refractive index and the number of particles becomes nonlinear [26–30]. For volume fractions up to 5%, it is possible to derive a simple and nonlinear expression [22,25,31] for the effective refractive index. For higher particle volume fractions the effective complex refractive index can be obtained by taking into account the positional correlations between the scattering particles. In this way, the imaginary part depends explicitly on the radial distribution function $g(r)$, describing the distribution of the particles, and its spherical Fourier transform, the structure factor $S(q)$ describing the light scattering of the particles. Here, $r$ is the distance from the center of a particle and $q$ the scattering wavenumber [27,29,32,33]. These correlations have a prominent effect at high volume

fractions [6,7,13,19]. However, it was observed that the volume fraction dependence of the real part deviates only little from linearity [22,31,34–39]. It is therefore difficult to compare different models of the real refractive index to experimental results. Indeed, some authors noted the scarcity of experimental work on the effective refractive index [6,22,25,40]. Experimental evidence is particularly absent for high volume fractions of particles where colloidal suspensions easily become unstable [22].

A second complication is that measuring the real part of the refractive index of colloidal suspensions is challenging. For example, when measuring a colloidal suspension with an Abbe refractometer, the critical angle becomes ambiguous [36,41]. In this case, the Fresnel equations need to be modified to take into account the particulate nature of the medium [24,30,42,43]. When measured in transmission, for example, through strongly forward scattering media such as tissue [44], the partially coherent diffusive light makes a quantitative determination of the real part of the refractive index ambiguous. In that case, coherence gating may be applied to filter the diffusive light from the ballistic light [27,44,45].

The work presented in this paper consists of experimental results and theoretical analysis of the complex refractive index of dense suspensions of 100 nm silica particles in water. Experimentally, we determine the group index, group velocity dispersion (GVD), and scattering attenuation with a spectral domain Mach-Zehnder interferometer over a broad wavelength range.

The experimental data is compared to two volume fraction dependent models for the complex effective refractive index of dense colloidal suspensions. The first model is the quasi-crystalline approximation (QCA) of the Foldy-Lax equations in the low frequency limit described by Ding and Tsang [7]. The second is the coupled dipole model (CDM) by Parola *et al.* [6]. CDM is conceptually similar to the coupled dipole method to computationally obtain the scattering properties [46], or thermal radiation [47,48] of an arbitrarily shaped particle.

We observe that the nonlinear response of the GVD to the particle size and concentration is much larger than that of the group index of the suspension. From a fit of the CDM model to the full complex refractive index over a large size parameter and concentration range we obtain the mean particle size, size polydispersity, and refractive index. We show that the obtained size distribution is in good agreement with a reference measurement.

## 2. THEORY

### A. Refractive Index of Dilute Suspensions

The complex refractive index is defined as

$$\tilde{n}(k) = n(k) + i\frac{\mu(k)}{2k}, \tag{1}$$

with the real part $n(k)$ related to the phase velocity of a wave propagating through a medium and the imaginary part related to the attenuation of the wave in the medium. Here, $k$ is the wavenumber in vacuum, and $\mu$ the attenuation coefficient, both due to absorption and scattering. In a non-absorbing medium and with non-absorbing particles, the attenuation coefficient is given only by the scattering attenuation coefficient $\mu_s$.

In a dilute suspension of particles the effect of the spatial correlations of particle positions can be neglected. In that case, the real part of the refractive index of a mixture of two components is, for many mixtures, well approximated with the Arago-Biot mixing formula. This equation expresses the refractive index as the average refractive index of both components weighted by their volume fraction [3]:

$$\mathrm{Re}\{\tilde{n}_{\mathrm{eff}}\} = f_v \mathrm{Re}\{\tilde{n}_p\} + (1 - f_v)\mathrm{Re}\{\tilde{n}_m\}. \tag{2}$$

Here, $f_v$ is the volume fraction of suspended particles, $\mathrm{Re}\{\tilde{n}_{\mathrm{eff}}\}$ is the real part of the complex effective refractive index of the suspension, and $\mathrm{Re}\{\tilde{n}_m\}$ and $\mathrm{Re}\{\tilde{n}_p\}$ are the real refractive indices of the embedding medium and of the suspended particles.

In dilute suspensions, $\mu_s$ is equal to the concentration times the scattering cross section. Therefore, it scales linearly with volume fraction. The full refractive index of a dilute suspension of a mixture of particles with different sizes can be calculated from the Mie scattering amplitude $S_{\mathrm{Mie}}$ through the van de Hulst refractive index [15,16,49]:

$$\tilde{n}_{\mathrm{eff}}(k) = n_m(k) - \sum_i^{N_s} \frac{3i n_p(k) f_{v,i}}{2x_i^3} S_{\mathrm{Mie},i}(\theta = 0). \tag{3}$$

Here, the refractive index of the suspension $\tilde{n}_{\mathrm{eff}}(k)$ is given by the refractive index of the embedding medium $n_m(k)$ minus a sum over all particle size bins with volume fraction $f_{v,i}$ per size bin. The sum consists of the refractive index of the particle $n_p(k)$, the size parameter $x_i = k_m a_i$, $k_m$ is the wavenumber in the embedding medium $n_m k$, $a_i$ is the particle radius, and the complex Mie angular scattering amplitude in the forward direction is $S_{\mathrm{Mie}}(\theta = 0)$. For unpolarized light $S_{\mathrm{Mie}}(\theta = 0)$ is the average of both angular scattering amplitudes $S_1$ and $S_2$. The angular scattering function is normalized such that $\mathrm{Re}\{S(\theta = 0)\} = \frac{k^2\sigma_s}{4\pi n_m}$, where the scattering cross section of the particle $\sigma_s$ is given according to Mie theory [50,51]. Both the van de Hulst refractive index and the Arago-Biot mixing formula scale linearly with the volume fraction of colloids.

### B. Electric Field in Dense Suspensions

To describe the complex refractive index for dense media the effect of the particle positions has to be taken into account in the electromagnetic field $\boldsymbol{E}(\boldsymbol{r})$ propagation through the medium.

The starting point here is the Foldy-Lax equation [10,52,53]

$$\boldsymbol{E}(\boldsymbol{r}) = \boldsymbol{E}_{\mathrm{inc}}(\boldsymbol{r}) + \sum_i \int_V \overleftrightarrow{G}_m(\boldsymbol{r} - \boldsymbol{r}')\, U_i(\boldsymbol{r}')\, \boldsymbol{E}(\boldsymbol{r}')\, \mathrm{d}\boldsymbol{r}', \tag{4}$$

with the field at every particle location $\boldsymbol{r}_i$ given by

$$\boldsymbol{E}(\boldsymbol{r}_i) = \boldsymbol{E}_{\mathrm{inc}}(\boldsymbol{r}_i) + \sum_{j\neq i} \int_V \overleftrightarrow{G}_m(\boldsymbol{r}_i - \boldsymbol{r}')\, U_j(\boldsymbol{r}')\, \boldsymbol{E}(\boldsymbol{r}')\, \mathrm{d}\boldsymbol{r}', \tag{5}$$

with $\boldsymbol{E}$ the total field, and $\boldsymbol{E}_{\mathrm{inc}}$ the external excitation field. The Green's dyadic operator of the embedding medium $\overleftrightarrow{G}_m$ is given by [53]

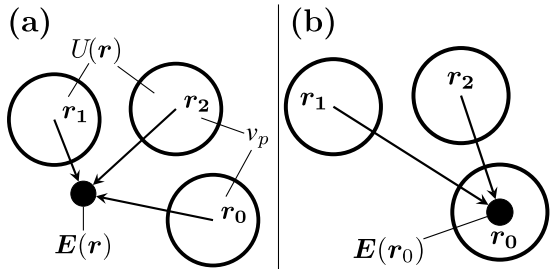


**Fig. 1.** Sketch of the Foldy-Lax equations. (a) The field at position $\boldsymbol{r}$ is the sum of the field radiated by all particles. (b) The field at the particle at position $\boldsymbol{r}_0$ depends on the radiated field from surrounding particles.

$$\overleftrightarrow{G}_m(\boldsymbol{r}) = \left(\overleftrightarrow{I} + \tfrac{1}{k_m}\nabla\otimes\nabla\right)\frac{e^{ik_m|\boldsymbol{r}|}}{4\pi|\boldsymbol{r}|}. \tag{6}$$

Here, $\overleftrightarrow{I}$ is the identity matrix and $U_i(\boldsymbol{r})$ is the scattering potential given by the refractive index contrast from the particle at position $\boldsymbol{r}_i$ and is given by $U_i(\boldsymbol{r}) = (m^2-1)k_m^2$ inside a particle volume $v_i$ and is zero within the embedding medium, and $m$ is the refractive index contrast of the particle $n_p/n_m$. The electromagnetic propagation is sketched in Fig. 1. Here, the Foldy-Lax equations are sketched for three particles at positions $\boldsymbol{r}_{0-2}$. In Fig. 1(a) the interactions as described in Eq. (4) are shown. The electric field at position $\boldsymbol{r}$ is given by the scattered field of all other particles and the external field $\boldsymbol{E}_{\text{inc}}(\boldsymbol{r})$. For this, the field of all particles must be known. The field for the particle at position $\boldsymbol{r}_0$ is given by the external field $\boldsymbol{E}_{\text{inc}}(\boldsymbol{r})$, and the field scattered by all other particles is given by Eq. (5), which is sketched in Fig. 1(b).

The total field $\boldsymbol{E}$ appears on both sides of Eq. (5). In the Born approximation the electric field in the right hand side is set to $\boldsymbol{E}(\boldsymbol{r}) = \boldsymbol{E}_{\text{inc}}(\boldsymbol{r})$. The exact solution of the Foldy-Lax equations can then be obtained by taking the Born approximation as a first approximate for the electric field and iteratively solving for the total field for a system with a known spatial refractive index distribution $U(\boldsymbol{r}) = \sum_i U_i(\boldsymbol{r})$. For a correlated particulate medium in Brownian motion solving the Foldy-Lax equations would require averaging over all known particle positions. These can be obtained from a Monte Carlo simulation.

### C. Quasi-crystalline Approximation

The spatial correlations between scatterers can be taken into account with the quasi-crystalline approximation (QCA). To get the field at the particle $\boldsymbol{E}(\boldsymbol{r}_0)$, QCA replaces the contribution of all other particles $\boldsymbol{r}_{i\neq 0}$ to the electric field at particle position $\boldsymbol{r}_i$ with the scattered field of an average particle at position $\boldsymbol{r}_j$ weighted by the radial distribution function $g(|\boldsymbol{r}_i - \boldsymbol{r}_j|)$. The Foldy-Lax equations under the QCA are

$$\langle \boldsymbol{E}(\boldsymbol{r})\rangle = \boldsymbol{E}_{\text{inc}}(\boldsymbol{r}) + N\int_V \overleftrightarrow{G}_m\left(\boldsymbol{r}-\boldsymbol{r}'\right) U_0\left(\boldsymbol{r}'\right)\left\langle \boldsymbol{E}_0\left(\boldsymbol{r}'\right)\right\rangle \mathrm{d}\boldsymbol{r}' \tag{7}$$

and

$$\langle \boldsymbol{E}_0(\boldsymbol{r})\rangle = \boldsymbol{E}_{\text{inc}}(\boldsymbol{r}) + (N-1) \times \int_V \overleftrightarrow{G}_m\left(\boldsymbol{r}-\boldsymbol{r}'\right) U_0\left(\boldsymbol{r}'\right) g\left(\left|\boldsymbol{r}-\boldsymbol{r}'\right|\right)\left\langle \boldsymbol{E}_0\left(\boldsymbol{r}'\right)\right\rangle \mathrm{d}\boldsymbol{r}'. \tag{8}$$

Here, $N$ is the number of particles, $\langle \boldsymbol{E}_0(\boldsymbol{r})\rangle$ the average field of a particle, and $U_0(\boldsymbol{r})$ the potential of a single particle at position $\boldsymbol{r}$.

When propagating waves are considered, it is useful to express the radial distribution function $g(r)$ as its spherical Fourier transform: the structure factor $S(q)$. Here, $q = 2k_m\sin(\frac{1}{2}\theta)$ is the scattering wavenumber and $\theta$ the scattering angle. The spatial correlations between particles of different species or in different size bins are encoded in the partial structure factor $S_{i,j}(q)$. A general expression for the partial structure factor of polydisperse hard sphere particles in the Percus-Yevick approximation [54] is given by Tsang *et al.* [55] [Eqs. (8.2.7)–(8.2.19) p. 413].

### D. QCA in the Small Scattering Angle Limit

Equations (7) and (8) can be solved for small size parameters in the small scattering angle limit ($\theta \to 0$), also called the low frequency limit ($q \to 0$) [56]. For a polydisperse particle size distribution, the solution for the complex refractive index $\tilde{n}_{\text{eff}}$ is presented by Ding and Tsang [7] as

$$\tilde{n}_{\text{eff}}^2 = n_m^2 + \frac{3n_m}{D}\sum_i^{N_s} f_{v,i}\, y_i \left\{1 + \frac{2in_m^2k^3}{3D} \times \left[a_i^3 y + \sum_j^{N_s} 8\pi^3 a_j^3 \rho_j y\left(1 - S_{i,j}(q=0)\right)\right]\right\}. \tag{9}$$

Here, $N_s$ is the number of size bins and the indices $i$, $j$ denote the size bins. The concentration of particles of size bin $j$ is $\rho_j$, $f_{v,i}$ is the volume fraction of particles with radius $a_i$, and the parameters $y$ and $D$ are given by

$$y = \frac{n_p^2 - n_m^2}{n_p^2 + 2n_m^2} \quad \text{and} \quad D = 1 - \sum_i^N f_{v,i}\, y. \tag{10}$$

The expression Eq. (9) is henceforth referred to as the low frequency QCA (LF-QCA) model.

### E. Coupled Dipole Model

A different approach to obtain the effective refractive index in a scattering medium is to consider the individual molecules that make up a particle as discrete dipole scatterers. The field at the discrete dipole at position $\boldsymbol{r}_i$ is given by

$$\boldsymbol{E}_i(\boldsymbol{r}) = \boldsymbol{E}(\boldsymbol{r}) + \alpha_d \sum_{i\neq j} \overleftrightarrow{G}_d(\boldsymbol{r})\boldsymbol{E}_i(\boldsymbol{r}_j). \tag{11}$$

Here, $\alpha_d$ is the polarizability of a dipole and $G_d$ is the Green's dyadic of a dipole given by

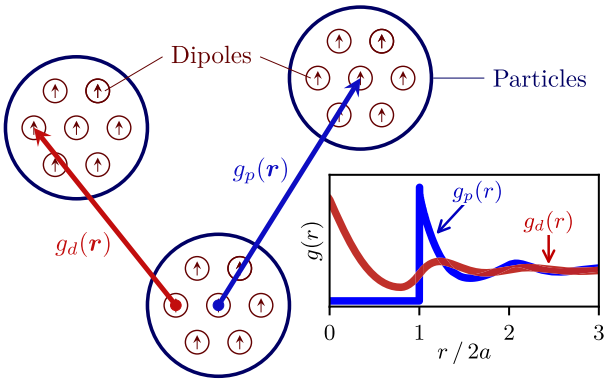


**Fig. 2.** Sketch of the coupled dipoles, the scattering particles, and the radial distribution function of the particles $g_p(r)$ (blue) and the discrete dipoles $g_d(r)$ (red).

$$\overleftrightarrow{G}_d(\boldsymbol{r}) = \left[\left(3\hat{\boldsymbol{r}}\otimes\hat{\boldsymbol{r}} - \overleftrightarrow{I}\right)\left(\frac{1}{k_m^3 r^3} - \frac{i}{k_m^2 r^3}\right) \times \frac{1}{k_m r}\left(\hat{\boldsymbol{r}}\otimes\hat{\boldsymbol{r}} - \overleftrightarrow{I}\right)\right] \times \exp(ik_m|\boldsymbol{r}|). \tag{12}$$

If the particles are considered to be a continuum of dipoles, and the quasi-crystalline approximation is applied, the sum in Eq. (11) is replaced with an integral similar to Eq. (8). This is given by

$$\boldsymbol{E}(\boldsymbol{r}_i) = \boldsymbol{E}_{\text{inc}}(\boldsymbol{r}_i) + \alpha \int_V g_d\left(|\boldsymbol{r}-\boldsymbol{r}'|\right)\overleftrightarrow{G}_d\left(\boldsymbol{r}-\boldsymbol{r}'\right)\boldsymbol{E}\left(\boldsymbol{r}'\right)\mathrm{d}\boldsymbol{r}'. \tag{13}$$

Here, $\alpha$ is the polarizability per volume, and $g_d(r)$ the dipole radial distribution function.

A solution to Eq. (13) was obtained by Parola *et al.* [6]. The field of two counterpropagating waves was chosen as ansatz for the field $\boldsymbol{E}(\boldsymbol{r}_i)$, and the external field $\boldsymbol{E}_{\text{inc}}$. The complex refractive index was obtained from the consistency conditions required to solve Eq. (13) for a correlated dipole fluid.

In this model, the dipoles are embedded in a particle, as shown in Fig. 2. Therefore, the radial distribution function of the dipoles $g_d(r)$ depends on correlations within the same particle, and correlations with dipoles in nearby particles. The intra-particle correlation function $g_{\text{intra}}(r)$ between two dipoles within a particle is given by convolution of the particle shape by itself, i.e.,

$$g_{\text{intra}}(r) = s(r) * s(r), \tag{14}$$

with the particle shape function $s(r)$ for a spherical particle with volume $v_p$ given by

$$s(\boldsymbol{r}) = \frac{1}{v_p}\left(1 - \Theta(|\boldsymbol{r}-a|)\right). \tag{15}$$

The inter-particle contribution $g_{\text{inter}}(r)$ is given by

$$g_{\text{inter}}(r) = s(r) * s(r) * g_p(r). \tag{16}$$

The dipole radial distribution function $g_p(\boldsymbol{r})$ is the sum of both the inter-particle and the intra-particle contributions, i.e.,

$$g_d(r) = g_{\text{inter}}(r) + g_{\text{intra}}(r) = s(r) * s(r) * g_p(r) + s(r) * s(r). \tag{17}$$

In the Fourier domain, this convolution can be written as a multiplication of the particle structure factor $S_p(q)$ and the spherical Fourier transform of the particle volume squared. The dipole structure factor $S_d(q)$ is then given by

$$S_d(q) = F^2(q)S_p(q) + 1. \tag{18}$$

Here, $F(q)$ is the form factor of the particle, which is a Fourier transform of the particle shape. For a spherical particle this is given by

$$F(q) = \frac{4\pi}{v_p}\int \frac{r\sin(qr)}{qr}\left(1 - \Theta(r-a)\right)\mathrm{d}r = 3\frac{\sin(qa) - qa\cos(qa)}{(qa)^3}. \tag{19}$$

For a particle size distribution with size bins $i$ with radius $a_i$, the partial form factor $F_i(q)$ and partial structure factor $S(q)$ can be geometrically averaged over the particle density per size bin with number density $\rho_i$ [33]:

$$\left\langle a^3F^2(q)S_p(q)\right\rangle_{\text{PSD}} = \frac{\sum_{ij}(a_ia_j)^{3/2}F_i(q)F_j(q)S_{i,j}(q)\sqrt{\rho_i\rho_j}}{\sum_i \rho_i}, \tag{20}$$

with $S_{i,j}(q)$ the structure factor of size bin $i$, $j$. The real part of the effective refractive index $n_{\text{eff}}$ of the suspension is then given by [6]

$$\mathrm{Re}\{\tilde{n}_{\text{eff}}\} = n_m + f_v n_m\left(n_p - n_m\right) + \frac{f_v n_m}{2}\left(\frac{f_v-1}{3} + \frac{C_r}{\pi}\right)\left(\frac{n_p-n_m}{n_m}\right)^2, \tag{21}$$

with

$$C_r = \frac{1}{3k_m^3}\int_0^\infty \left\langle a^3F^2(q)S(q)\right\rangle_{\text{PSD}} \times\left[\frac{8}{3}k_m^3q - k_mq^3\left(2k_m^4 - k_m^2q^2 + \frac{q^4}{4}\right)\ln\left(\frac{q+2k_m}{|q-2k_m|}\right)\right]q\mathrm{d}q. \tag{22}$$

The correlation integral $C_r$ encodes nonlinear scattering effects on the real part of the refractive index. It is dependent on the particle volume fraction through the structure factor $S(q)$.

The imaginary part of the effective refractive index is an integral over the product of the scattering amplitude $f(q)$ and the structure factor over all scattering angles ($q \le 2k_m$). For a particle size distribution this is given by Vrij [29,33] as

$$\mu_s = 2k\,\mathrm{Im}\{n_{\text{eff}}\} = 2\pi\int_0^\pi \sum_{i,j}^N \sqrt{\rho_i\rho_j}\,f_i(\theta)f_j(\theta)S_{i,j}(\theta)\sin(\theta)\mathrm{d}\theta. \tag{23}$$

The scattering amplitude $f_i(q)$ for a particle in size bin $i$ can be calculated with the particle form factor $F_i(q)$ through [6]

$$f^2(q) = \frac{\alpha_p^2v_p^2F^2(q)\left(8k_m^4 - 4k_m^2q^2 + q^4\right)}{8n_m^2}, \tag{24}$$

where $v_p$ is the particle volume and $\alpha_p$ is the dimensionless particle polarizability relative to the embedding medium, which is given by

$$\alpha_p = \frac{3}{4\pi}\left(\frac{(n_p - n_m + 1)^2 - 1}{(n_p - n_m + 1)^2 + 2}\right). \tag{25}$$

The aim of this work is to experimentally test the predictions given by Eqs. (3), (9), (21), and (23) for the concentration dependence of both parts of the complex refractive index. Here, the latter two Eqs. (21) and (23) are used together to provide the real and imaginary parts of the CDM.

## 3. METHODS

### A. Experimental Setup

Optical properties of colloidal suspensions were measured with an optical setup based on a Mach-Zehnder interferometer. This setup is described in detail in our previous work [57]. In summary, the visible part of the spectrum with wavelengths between 400 nm and 950 nm emitted by a supercontinuum laser (EVO EUL-10, NKT) is split into the sample arm and the reference arm of the interferometer by a 10-90 beamsplitter (BS025, Thorlabs) and recombined with a 50-50 beamsplitter (BS013, Thorlabs). The spectrum is measured with a spectrometer (FX VIS-NIR, Ocean Optics). The intensity in each arm was measured separately indicated by $I_{\mathrm{sam}}(k)$ and $I_{\mathrm{ref}}(k)$ for the sample arm and reference arm, respectively. The spectrum measured with both the arms open is given by $I_{\mathrm{tot}}(k)$.

The volume fractions of the prepared silica samples varied from 0.05 to 0.36. The samples were prepared from a stock sample of 0.5 volume fraction 100 nm silica particles (Levasil, Nouryon). This was diluted with demineralized water (Milliq 15 MΩcm) to eight samples with volume fractions ranging from 0.05 to 0.4. In order to make sure the particles behave as hard spheres, 0.2 ml salt solution was added to each sample to lower the zeta potential. The salt solution was prepared with 400 ml demineralized water and 0.95 g NaCl.

The sample was measured in a 1000 μm flow cell (45/Q/1, Starna). The mixture was introduced to the flow cell by a BD10 luer lock syringe. Before each measurement the previous sample was flushed out by water and air. Between each two measurements a calibration measurement with demineralized water was performed. In addition to the interference spectrum, the transmission spectra of the sample arm and the reference arm were measured.

The spectra were obtained with an exposure time that was varied between 200 μs and 1000 μs, depending on the transmission of the sample. The number of spectra acquired was 1000, except for the measurement at $f_v = 0.36$ where it was set to 10,000.

The variance of the attenuation measurements was determined with Intralipid 20% dilutions with similar attenuation coefficients as the samples of silica particles. These were 11 to 13 measurements of Intralipid for the volume fractions of 0.5 vol. %, 1 vol. %, and 2 vol. % of Intralipid 20% in water. The standard deviation was determined as a function of wavenumber $k$ and attenuation $\mu$. The standard deviation for a particular silica particle solution measurement was determined with the weighted average of the nearest two measured Intralipid attenuations. Since the transmission spectra of Intralipid differ from those for silica, this was done per wavenumber. The combined results of the Intralipid measurement are the wavelength and attenuation dependent standard deviation of the attenuation of the silica samples $\sigma_\mu(\mu_s(k), k)$.

### B. TEM Particle Analysis

The PSD of the particles that were used in this experiment was determined with transmission electron microscopy (TEM) analysis. The TEM images were imaged with a Talos L120C microscope operated at 120 kV. The TEM samples were prepared by drop-casting of the particle solution onto a carbon-formvar coated Cu TEM grid. An example of an acquired TEM image is shown in Fig. 3(a). First, the noise in the images was reduced with a convolution with a small square kernel of 5 pixels. Second, local outlying intensity peaks were removed by morphologically opening and subsequently closing the negative image with the same kernel. Third, the particles were selected from the image with a circular Hough transform from the OpenCV package [58], as is shown in Fig. 3(b). In total 7730 particles were analyzed in four micrographs. The particle diameter was determined from the area of the particles in pixels on the micrograph. This area was determined from the binarized TEM image, which is overlaid on top of the micrograph in Fig. 3(c). The cutoff pixel value was determined using Otsu's method [59]. A pixel is counted towards the area of a particle if it is within the Hough radius with a margin of 3 pixels and the pixel is in the binarized image.

### C. Phase and Amplitude Analysis

The analysis of a single measurement is summarized in the flow chart shown in Fig. 4. The analysis is similar to our previous work [57].

The spectra $I_{\mathrm{tot}}$, $I_{\mathrm{sam}}$, and $I_{\mathrm{ref}}$ are obtained in the wavelength domain. The wavelengths that are used in the analysis are between 410 nm and 930 nm. The spectra were interpolated to the wavenumber domain to an array size of 8192.

The scattering attenuation $\mu_s(k)$ is determined in steps 1 and 2 of the flow chart from the measured optical transmission divided by the transmission spectrum with demineralized water. The transmission spectrum of a sample with 5 vol. % particles and its calibration with water are shown in Fig. 5(a). The source

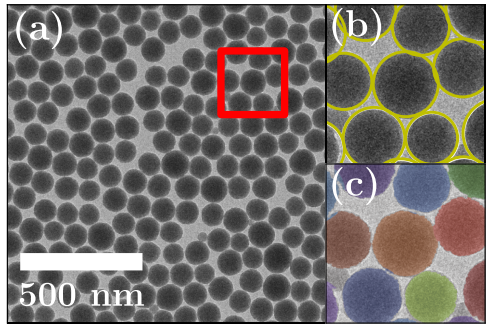


**Fig. 3.** (a) TEM image of the silica particles. (b) The yellow circles show the particle circumference obtained with a Hough transform. (c) Segmented particles. Pixels with the same color are associated with the same particle.

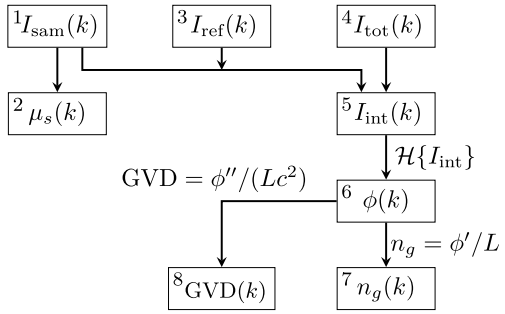


**Fig. 4.** Flow chart of the analysis of a single interference spectrum measurement. $\mu_s(k)$, $n_g(k)$, and GVD$(k)$ (steps 2,7,8) are obtained from $I_{sam}(k)$, $I_{ref}(k)$, and $I_{tot}(k)$ as indicated in the main text.

spectrum $I_{source}(k)$, the splitting ratio, and the losses of the setup itself are divided out with a calibration measurement of the transmission spectrum of water, where $\mu_s(k) = 0$. The transmission, obtained from the ratio between the spectra in Fig. 5(a), is shown in Fig. 5(c).

The interference spectrum $I_{int}(k)$ is calculated from the total spectrum $I_{tot}$ with $I_{int}(k) = I_{tot}(k) - (I_{sam}(k) + I_{ref}(k))$ (step 5). The measured spectrum of the same sample with a blocked reference arm is shown in Fig. 5(b). The phase spectrum $\phi(k)$ is obtained from the Hilbert transform of $I_{int}(k)$ and fit to a third order polynomial (step 6). In the last steps, the group index and GVD are calculated from the fitted phase $\phi(k)$ with

$$n_g = n + k\frac{dn}{dk} = \frac{1}{L}\frac{d\phi}{dk} \tag{26}$$

and

$$\text{GVD} = \frac{2}{c^2}\frac{dn(k)}{dk} + \frac{k}{c^2}\frac{d^2n(k)}{dk^2} = \frac{1}{Lc^2}\frac{d^2\phi(k)}{dk^2}, \tag{27}$$

respectively. The group index $n_g(k)$ is related to the frequency of the calibrated interference signal $I_{int}(k)$. The GVD is related to the chirp of the same signal $I_{int}(k)$.

### D. Model-Based Analysis

The model-based analysis is based on two independent fitting routines: one for the refractive index and one for the attenuation coefficient. A flowchart of the forward fitting algorithm is shown in Fig. 6. The fitting routine is executed for every volume fraction.

In the refractive index routine the effective group refractive index as a function of wavenumber is calculated with either the LF-QCA or CDM scattering model. This loop uses a mean particle radius $\langle a \rangle$ and a phase index as initial input. The phase index of the particle is described by a polynomial expansion as

$$n_p(k) = n_0 + n_1 k + n_2 k^2 + n_3 k^3. \tag{28}$$

The initial polynomial parameters $n_{0-3}$ of the phase index were chosen for silica particles with a porosity of 15% based on Daimon and Masumura [60] and Malitson [61] for water and silica, respectively.

The initial radius $\langle a \rangle$ was set to 50 nm. For particles that are small compared to the wavelength, the polydispersity has a small effect on the effective refractive index. Therefore, to speed up the calculation, the effective refractive index is calculated for a monodisperse suspension with radius $\langle a \rangle$.

For the LF-QCA model, the phase index of the suspension $\text{Re}\{\tilde{n}_{eff}(k)\}$ was calculated from Eq. (9). The phase index for the CDM was calculated with Eq. (21). From the estimated phase index, the effective group index of the suspension was calculated from Eq. (26) and is compared to the measured group index.

An estimate of the phase index of the particles is obtained by minimizing the sum of the square difference for all volume fractions between the measured effective group index and the effective group index, as predicted from the refractive index

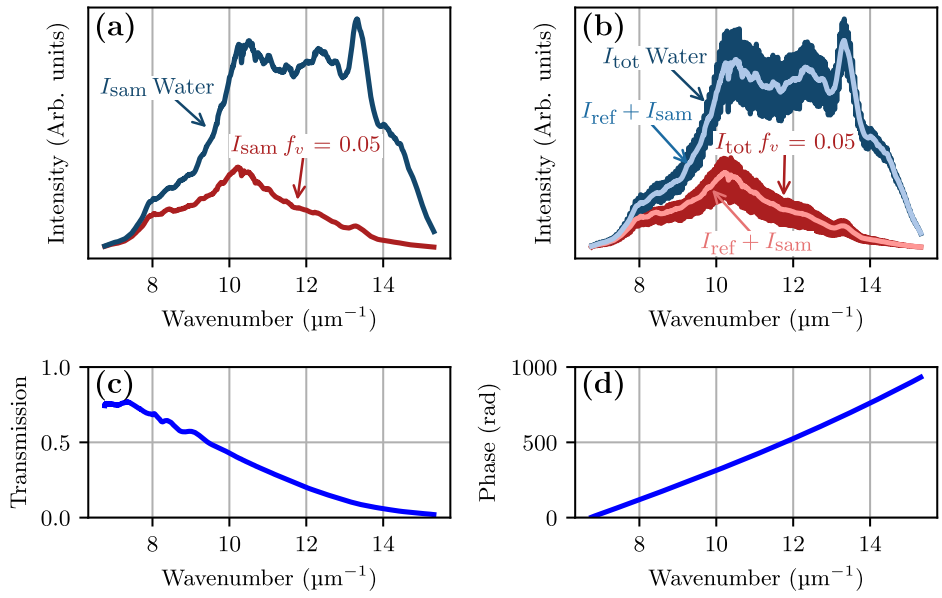


**Fig. 5.** Analysis steps of a sample with 5 vol. % silica particles and its calibration measurement. The sample arm intensity $I_{sam}(k)$ is shown in (a). The interference when both arms are open is shown in (b). (c) Transmission of the same sample and (d) spectral phase.

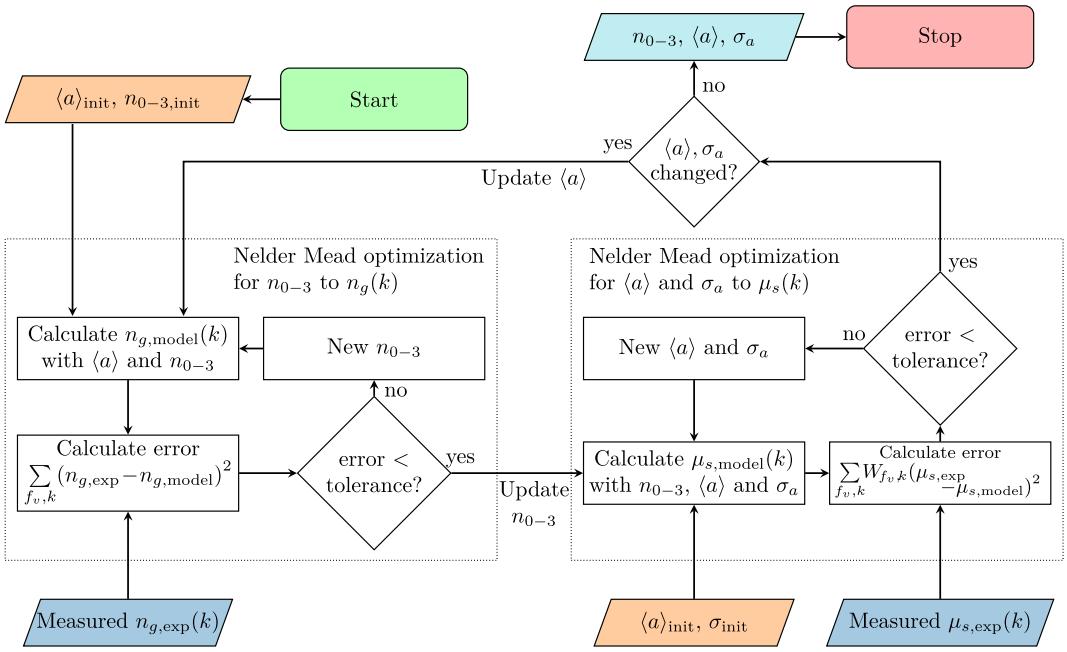


**Fig. 6.** Flow chart of the fitting procedure with the forward model. The parallelograms indicate the input and output. The measured data are shown in blue, initial values are shown in beige, and the fit parameters are shown in cyan.

model with volume fraction $f_v$ and radius $\langle a \rangle$ as input. In successive iterations the square error was minimized with Scipy's [62] Nelder-Mead algorithm [63] using the default precision.

After obtaining sufficiently close agreement between the modeled group index and the measured group index the algorithm switches to estimate the attenuation coefficient, indicated with the loop shown on the right in the flow chart. Here, the particle size distribution is obtained from a fit of $\mu_s(k)$ from the LF-QCA and CDM models to the attenuation with the estimated fit of the phase index from the previous loop. The particle size distribution was parameterized with a normal distribution with mean radius $\langle a \rangle$ and standard deviation $\sigma_a$. For the LF-QCA model, $\mu_s(k)$ was calculated from Eq. (9). For the CDM, $\mu_s(k)$ was calculated from Eq. (23). The error that was minimized is the square difference between the measured attenuation and the modeled attenuation with relative weights $W_{f_v,k} = 1/\sigma^2_{f_v,k}$, with $\sigma^2_{f_v,k}$ the variance in $\mu_s$ obtained from the Intralipid measurements. Similar to the case for the refractive index loop, the error was minimized with the Nelder-Mead algorithm. The initial polydispersity was set at 5% of the mean radius of $\langle a \rangle_{\text{init}}$.

The forward models for both $n(k)$ and $\mu_s(k)$ were computed on the wavelength range of 410 nm to 930 nm for 256 wavelengths. To compare with the measured scattering attenuation and group index, the measured data is interpolated to match the wavelengths of the forward fit. The scattering attenuation is calculated for 64 particle size bins within four standard deviations from the mean. This was done to make the quality of the sampling independent of the standard deviation of the particle radius $\sigma_a$.

The obtained mean particle radius $\langle a \rangle$ is transferred from the attenuation loop to the refractive index loop to calculate the polynomial parameters of the phase index $n_{0-3}$ of the particles with the refractive index models. This phase index is then used to update the PSD in the attenuation loop. This procedure is repeated until no further improvement in the estimated mean diameter and polydispersity could be achieved. In practice, the diameter and polydispersity often do not significantly change after the first two iterations, and do not change within machine precision after approximately the sixth iteration, depending on the used model.

After completion of the full optimization routine, the porosity $f_{v,\text{pores}}$ is calculated from the fitted phase index of the silica particles with the assumption that the pores fully consist of water. The porosity is then calculated with

$$f_{v,\text{pores}} = \left\langle \frac{n_{\text{fit}}(k) - n_{\text{bulk}}(k)}{n_{\text{water}}(k) - n_{\text{bulk}}(k)} \right\rangle_k, \tag{29}$$

where $n_{\text{bulk}}(k)$ is taken from Malitson [61] and $n_{\text{water}}(k)$ is taken from Daimon and Masumura [60].

### E. Estimation of the Confidence Interval

The confidence interval of the mean diameter $\langle a \rangle$ and polydispersity $\sigma_a$ is estimated from the weighted residue $R$:

$$R(\langle a \rangle, \sigma_a) = \sum_{f_v,k} W_{f_v,k}\left(\mu_{s,\text{exp},k,f_v} - \mu_{s,\text{fit},k,f_v}(\langle a \rangle, \sigma_a)\right)^2. \tag{30}$$

Here, $\mu_{\text{exp}}$ is the measured attenuation, $\mu_{\text{fit}}$ the fit, and $W$ the weights given by the Intralipid measurements. The region of confidence can be estimated as the region $R(\langle a \rangle, \sigma_a)$ that lies below a threshold $R_{\text{cutoff}}$ [64,65]:

$$R(\langle a \rangle, \sigma_a) \leq R_{\text{cutoff}}. \tag{31}$$

To heuristically find a reasonable $R_{\text{cutoff}}$, we fit $\langle a \rangle$ and $\sigma_a$ to an attenuation spectrum with one standard deviation offset given by

$$\mu_{\text{var}}(f_v, k) = \mu_{\text{exp}}(f_v, k) + \sigma_\mu(f_v, k)/\sqrt{N}. \quad (32)$$

Here, $\mu_{\text{var}}$ is the attenuation spectrum perturbed with the measured standard deviation, $N$ is the number of different measured volume fractions, which is eight, and $\sigma_\mu(f_v, k)$ is the standard deviation as determined from the Intralipid measurements. The $\langle a \rangle_{\text{var}}$ and $\sigma_{a,\text{var}}$ are the mean radius and polydispersity fitted to $\mu_{\text{var}}$. The cutoff residue $R_{\text{cutoff}}$ is then given by

$$R_{\text{cutoff}} = R\left(\langle a \rangle_{\text{var}}, \sigma_{a,\text{var}}\right). \quad (33)$$

The region of confidence for $\langle a \rangle$ and $\sigma_a$ is then given by Eq. (31).

## 4. RESULTS

### A. Real Part of the Effective Refractive Index

The measured group index and GVD for a volume fraction of $f_v = 0.36$ colloidal silica particles are shown in blue in Fig. 7. The result of the model-based analysis with the CDM model that best matches the data is shown in red. Because this is a result of a fit to all wavelength and volume fraction data, not just to the measurement at $f_v = 0.36$, a small offset from the group index data is present.

The volume fraction dependence of the model-based analysis of the group index is shown in Fig. 8 for the wavelengths 450 nm and 800 nm. Both $n_g$ and GVD are linearly dependent on volume fraction with no discernible nonlinearity in the group index data. The prediction from the CDM model is shown in red. The group index obtained with LF-QCA is not appreciatively different from CDM and is not plotted in Figs. 7 and 8. The measurement uncertainty is of similar size as the plot markers.

For the real part of the effective refractive index, the most significant discriminator between the CDM and LF-QCA effective refractive index models is the volume fraction dependence of the GVD. In Fig. 9 the measured GVD and the fitted GVD are shown for various wavelengths. For all wavelengths, with the exception of the GVD measured at wavelengths longer than 700 nm, the GVD is nonlinear with increasing particle volume fraction, particularly for lower wavelengths. It is remarkable that all models quantitatively match the data so well, despite the fact that the group index shown in Fig. 8 shows an almost perfect linear behavior. The volume fraction dependence of the GVD at a single wavelength is small compared to the difference in GVD between the lowest and highest measured wavelengths.

The CDM describes the measured GVD reasonably well for all wavelengths. It does have a constant offset at some wavelengths, but CDM clearly predicts a nonlinear behavior of the GVD with volume fraction. The GVD, as calculated with the

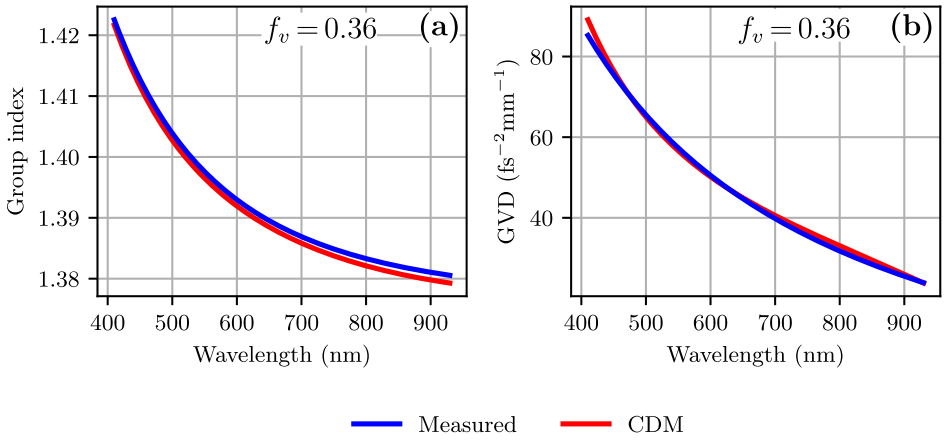


**Fig. 7.** Measured (a) group index and (b) GVD at different wavelengths compared to the Parola model for a volume fraction $f_v$ of silica particles in water.

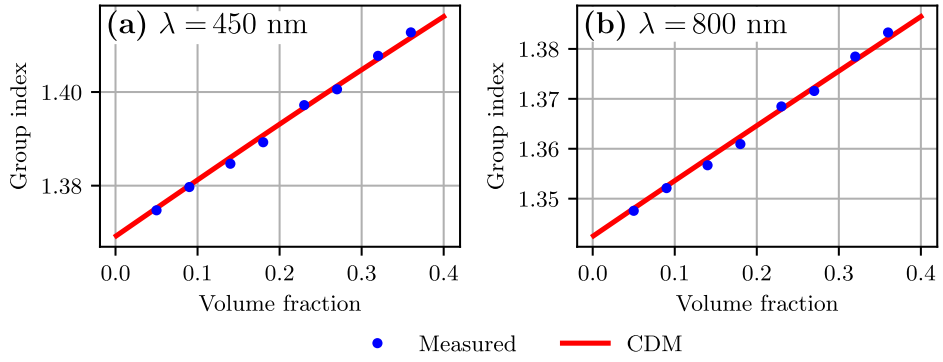


**Fig. 8.** Measured and modeled group index at (a) $\lambda = 450$ nm and (b) $\lambda = 800$ nm for different volume fractions of silica particles in water.

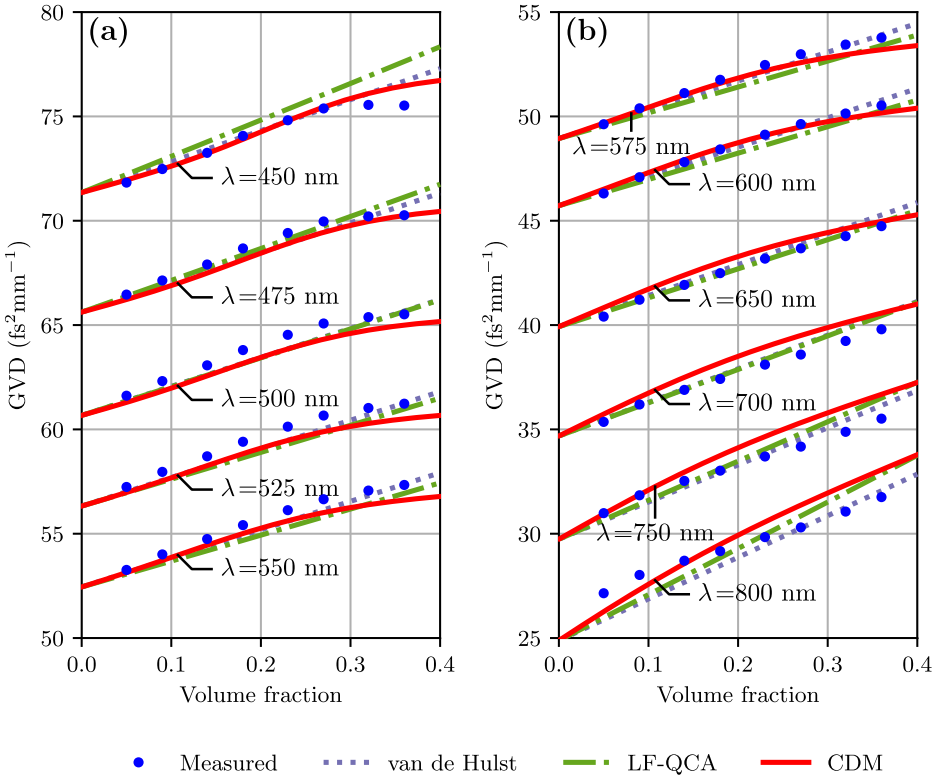


**Fig. 9.** GVD for various wavelengths and models. The CDM model describes the shape of the volume fraction dependence reasonably well. For low volume fractions the van de Hulst formula gives adequate results. At high wavelengths the size of the particle becomes small compared to the wavelengths, thus leading to a more linear increase of GVD with volume fraction.

LF-QCA and van de Hulst model, is indicated with the dotted lines in green and purple. The LF-QCA and van de Hulst models always predict a linear increase of the GVD with volume fraction, which is clearly not in good agreement with the data. Note that the phase index used for the van de Hulst model was taken to be the same as for the CDM. The uncertainty in the measurements is smaller than the plot markers.

The phase indices of the silica particles that are obtained with the CDM and LF-QCA models are shown in Fig. 10. Both models lead to a similar phase index. For comparison, the phase index of pure, nonporous silica is shown in black. The porosity, as obtained from the phase index of the particle obtained with the CDM, is 12.5%.

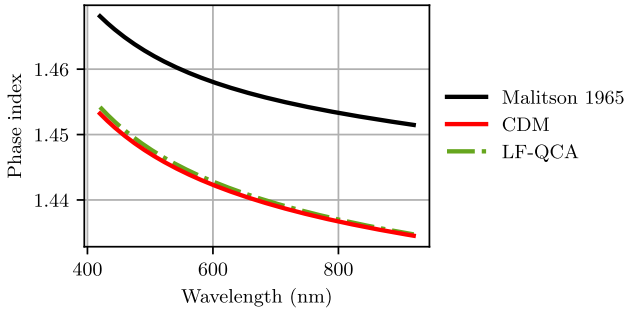


**Fig. 10.** Phase index of silica particles as determined with the various models from the model-based analysis compared to the phase index of nonporous silica (black).

### B. Imaginary Part of the Effective Refractive Index

The measured scattering attenuation $\mu_s(k)$ for the volume fractions of 0.05 and 0.36 as a function of wavelength is shown in Fig. 11, together with the CDM and LF-QCA model predictions. For comparison, the CDM prediction with the PSD obtained from the TEM analysis is also shown in Figs. 11 and 12. For the volume fraction of 0.05, CDM closely matches the measured attenuation, whereas the LF-QCA model overestimates the attenuation coefficient for shorter wavelengths. For higher volume fractions, it is the CDM that has an overestimation at lower wavelengths.

The differences for the various scattering models are more clearly visible when the scattering attenuation is visualized as a function of volume fraction, as shown in Fig. 12. For short wavelengths the higher attenuation results in more precise attenuation measurement (smaller error bars). For the wavelengths 450 nm and 500 nm the CDM model is very close to the measured attenuation. However, for longer wavelengths both the LF-QCA and the CDM underestimate the measured attenuation at high volume fractions. The volume fraction of maximum attenuation for the CDM is 17.0% at $\lambda = 450$ nm and 14.5% at $\lambda = 700$ nm. For the LF-QCA model this is 13.2%. The peak of the CDM is closer to the measured maximum.

The particle size distribution as obtained from the TEM analysis and the model-based analysis for $\langle a \rangle$ and $\sigma_a$ is shown

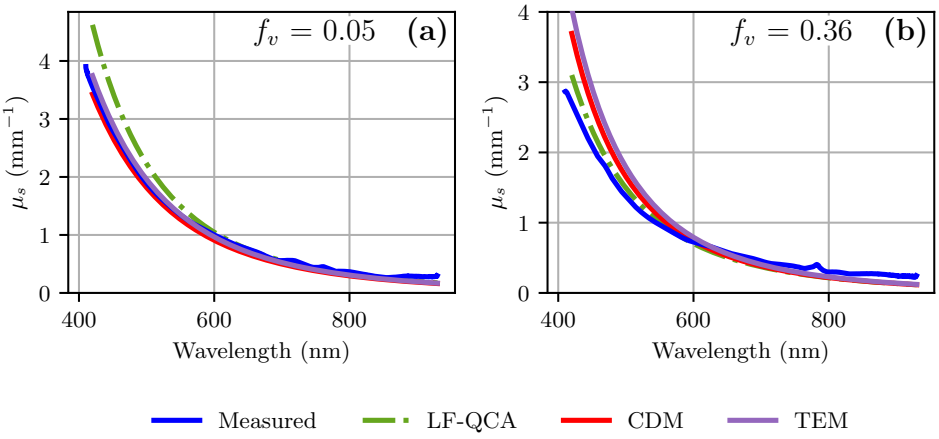


**Fig. 11.** Measured scattering attenuation $\mu_s(\lambda)$ compared with the fits with the various models. The CDM prediction of $\mu_s(\lambda)$ for the PSD obtained with TEM is shown in purple.

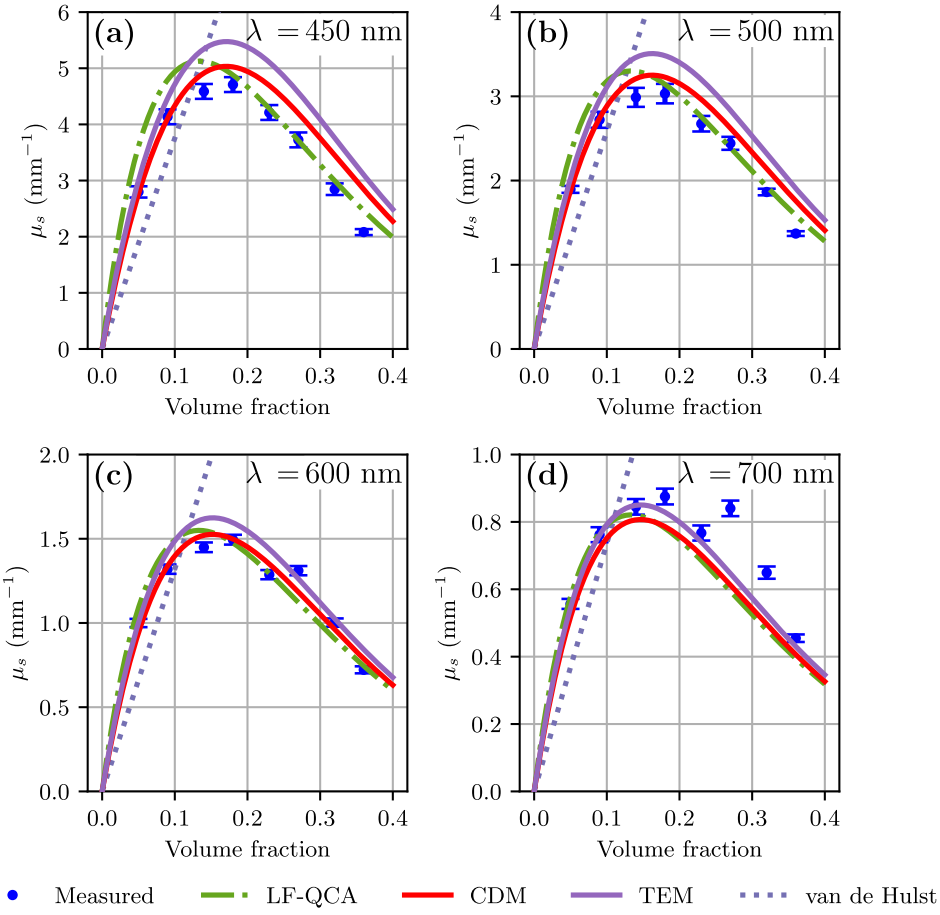


**Fig. 12.** Scattering attenuation as function of the volume fraction for four wavelengths.

in Fig. 13. The mean particle diameter as obtained with the CDM is 102.2 nm with confidence interval of (97.5 nm, 105.5 nm) with a polydispersity of 6.6% (1.7%, 13.4%). For the LF-QCA model this is 89.7 nm (79.7 nm, 96.9 nm). The polydispersity obtained with the LF-QCA model is 19.6% (15.4%, 25.4%). The mean size and polydispersity obtained from the TEM images are 99.7 nm and 9.4%.

## 5. DISCUSSION

### A. Comparison of Complex Refractive Index Models

To the best of our knowledge we are the first to compare experimental results with the CDM model. This is in contrast to the LF-QCA in the small scattering angle limit that is widely used to model the dependent scattering effect on both the imaginary

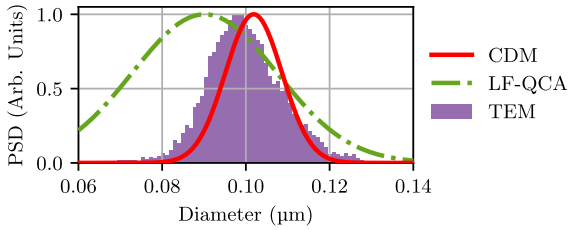


**Fig. 13.** Particle size distribution as determined with the model-based analysis compared with the distribution as obtained from TEM.

part [66,67] and the real part of the effective refractive index [22,38]. The CDM and LF-QCA have in common that for both models the effective complex refractive index scales nonlinearly with the volume fraction of the suspended particles.

The CDM accurately describes both the imaginary and real parts of the effective refractive index. It is particularly noteworthy that this model is able to predict reasonably well the nonlinear shape of the measured GVD curves. The LF-QCA model describes the real refractive index reasonably well, but does not predict a nonlinear volume fraction dependence of the GVD. Instead, it predicts a linear behavior, which is clearly not in agreement with the measurements.

The LF-QCA model performs poorly on inverting the measured attenuation spectra to a PSD, since for the LF-QCA model an increase of polydispersity and an increase of mean particle radius have a similar effect on the attenuation spectrum. For longer wavelengths, the LF-QCA model and the CDM provide similar results for the imaginary part of the refractive index. However, for shorter wavelengths, the prediction for the attenuation coefficient of the LF-QCA model is shifted upwards compared to the low volume fraction experimental data and the CDM. For high volume fractions and at low wavelengths, the LF-QCA model deviates less from the measured attenuation than the CDM.

The shape of the volume fraction dependence of the scattering attenuation as calculated with the LF-QCA model does not change with the size parameter. For example, the maximum attenuation is at $f_v = 0.13$ for all wavelengths. However, the experimental data shows that the volume fraction of maximum attenuation does depend on wavelength. This is visible in the CDM fit, where the peak of maximum attenuation varies with wavelength. The difference between the model predictions is due to the low frequency solution of the LF-QCA, which assumes a small particle size parameter $x$, which at $\lambda = 450$ nm with $x = 0.94$ is clearly violated.

The small particle assumption of the LF-QCA also complicates the retrieval of the PSD through the iterative model-based fit. Moreover, the mean diameter and the polydispersity are strongly correlated. Increasing the mean particle size or increasing the polydispersity has similar effects on the scattering attenuation and therefore cannot independently be determined. This effect is visible in the obtained PSD parameters where both the mean particle radius $\langle a \rangle$ and polydispersity $\sigma_a$ do not resemble well the ground truth obtained with TEM. The CDM model yields reasonable estimates for both the mean particle size and the polydispersity, as it encodes the effect of polydispersity on the attenuation better.

In addition to the low frequency LF-QCA and CDM models, we have tested the low frequency QCA with coherent potential (QCA-CP) [7] and Keller [13] models for the complex refractive index. The refractive index and attenuation predicted by QCA-CP is very similar to that as predicted by LF-QCA. The Keller model did not perform well for the attenuation, since the particles used in this work have a too low size parameter. Better results with the Keller model can be obtained with larger particles [68]. Interestingly, the Keller model predicts a quite strong volume fraction dependence on the GVD, which, however, does not match well to the data. The comparison with these models can be found in Supplement 1.

### B. Structural Correlation Effects on the Refractive Index

We have shown how dependent scattering encoded in the partial structure factor $S_{i,j}(q)$ affects the refractive properties of a colloidal medium. Both the real and imaginary parts of the effective refractive index are dependent on concentration through the structure factor. We believe we are the first to measure a nonlinear dependence of the real part of the effective refractive index on the particle volume fraction. Previous work was limited to the liquid-crystal phase transition of a colloidal crystal. For example, Okubo [40] measured an increase in the refractive index due to a phase transition in a dense colloidal medium. However, no comparison with a refractive index model was made, and no nonlinear concentration dependence in the liquid phase, other than the phase transition, was observed.

The experiments presented in this work were performed to a high degree with hard sphere particles. This has the advantage that a clear comparison with the theory can be made through the Percus-Yevick approximation of the structure factor. Hence, other structures, such as non-spherical particles, may give rise to different optical properties [69,70], but can be described using the same formalism as long as the structure factor is known. Furthermore, the ionicity of the fluid strongly influences the interactions. For example, a lower salt concentration can give rise to an artificially high volume fraction [40,71], since the particles occupy a higher effective volume due to the repellent inter-particle force. At a given particle volume fraction, this would lead to a stronger effective nonlinear effect on the GVD. In this case, the hard sphere potential would need to be replaced by a potential based on the zeta potential of the particle for obtaining an accurate structure factor.

### C. Scattering Form Factor

Parola *et al.* provided a concentration dependent scattering amplitude $f_{\mathrm{CDM}}(q)$ given by Eq. (24) that is approximately equal to the Mie scattering amplitude $f_{\mathrm{Mie}}(q)$, shown in Fig. 14(a). In the Rayleigh regime, the differences between these scattering amplitudes are negligible. However, for larger particles, evaluation of Eq. (23) with the approximate $f_{\mathrm{CDM}}(q)$ gives a slightly lower attenuation than expected from the Mie solution, as can be seen in Fig. 14(b). When the Mie scattering amplitude is used, the estimated PSD is only slightly closer to the PSD as obtained with TEM: the Mie-based PSD has a mean diameter of 100.7 nm and a polydispersity of 6.4%. However,

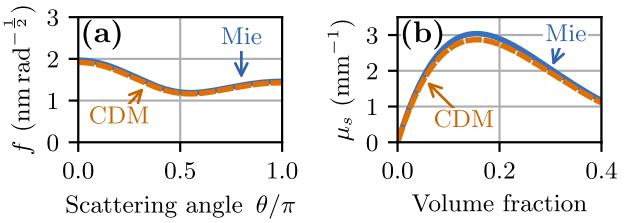


**Fig. 14.** (a) CDM scattering amplitude $f_{\mathrm{CDM}}(\theta)$ compared with the Mie form factor $f_{\mathrm{Mie}}(\theta)$ for monodisperse 100 nm particles at $\lambda = 500$ nm with a refractive index as measured in this work. In (b) the corresponding attenuation is shown.

this result does not significantly differ from the PSD as obtained with the scattering amplitude of Eq. (24). Therefore, the particles used in this work were small enough to be well described with the CDM scattering amplitude.

To use the CDM for larger particles, the Mie scattering amplitude is more accurate. However, incorporation of the Mie phase function in CDM as used in Eq. (22) is not possible due to the integration boundaries spanning an infinite $q$ range. An *ad hoc* solution would be to split the form factor such that for $q < 2k_m$ the Mie scattering amplitude $f_{\mathrm{Mie}}$ is used and for $q \geq 2k_m$ the CDM scattering amplitude $f_{\mathrm{CDM}}$. However, in contrast to the calculation of the scattering attenuation, this would make not a measurable difference to the real part of the refractive index.

### D. Effects of Polydispersity

The group index calculations were performed for a monodisperse particle size distribution and not by the polydisperse PSD used in the attenuation loop. This choice is substantiated by the fact that calculations showed that any realistic polydispersity of the particle suspension has only a limited effect on the group index and the GVD, as can be seen in Fig. 15. Figure 15 shows that the GVD at the wavelengths of 500 nm and 600 nm is plotted for a monodisperse particle size distribution and a normal particle size distribution with a strong polydispersity of 20% for particles with an average diameter of 50 nm, 100 nm, and 200 nm and the same refractive index as measured for the silica particles as used in this work. Even for a polydispersity of 20%, the effect of the size distribution on the GVD is very low for diameters smaller than 100 nm. It also shows that for smaller particles the particle correlations encoded in $g(r)$ have a negligible effect on the GVD, as would be expected for a molecular mixture [57].

Although the concentration effect on the group index and GVD was rather small for 100 nm particles, it was large enough to fit the phase index and distinguish the behavior of the different models. For larger particles Parola *et al.* predicted a more prominent concentration dependence of the refractive index for size parameters $x$ between 1.5 and 2.0, particularly for a volume fraction higher than 0.3. This would correspond to particles with a diameter of 200 nm in Fig. 15. Therefore, it would be of

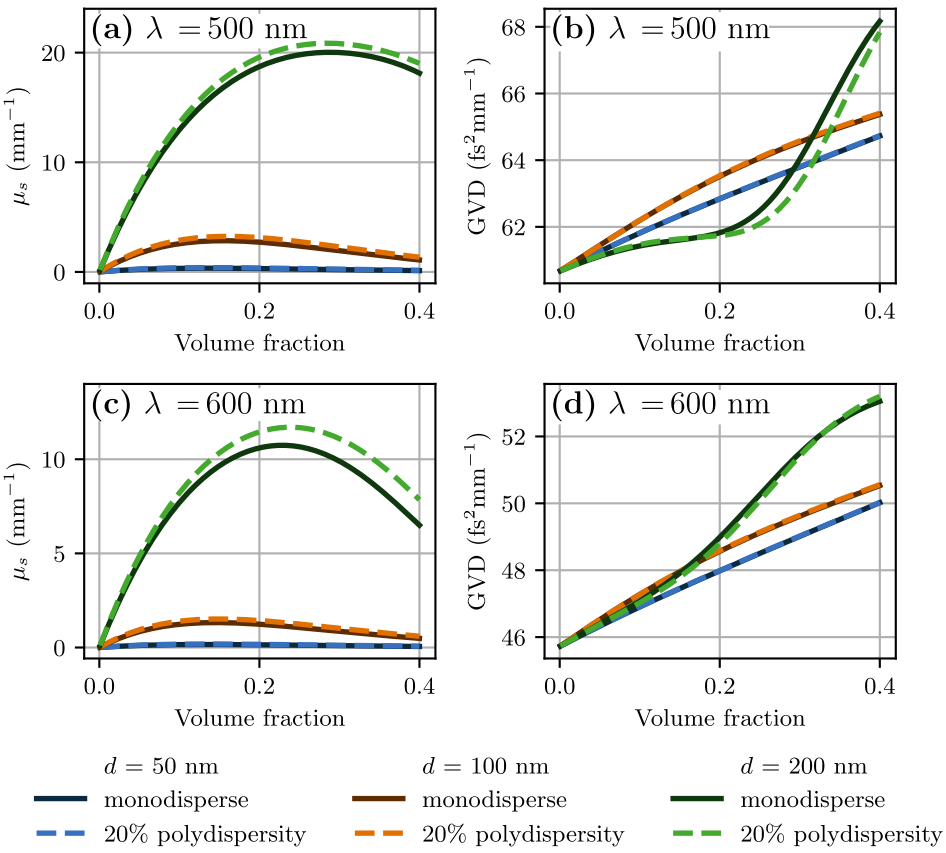


**Fig. 15.** CDM calculations of the concentration dependence of the (a,c) attenuation and (b,d) GVD for particles with a diameter of 50 nm, 100 nm, and 200 nm at the wavelengths of (a,b) 500 nm and (c,d) 600 nm.

interest to investigate the concentration dependence of larger particles.

### E. Measurement of Particle Properties

The refractive index, PSD, and porosity of a sample of silica nanoparticles were determined through a fit of the refractive index and particle properties. The mean particle size and polydispersity obtained with the LF-QCA model deviate significantly from those obtained with TEM. Better results are obtained with the CDM, where the PSD has a mean radius very close to that obtained with TEM. However, the estimated polydispersity is lower compared to the TEM images, albeit comparable. A main contributor to the size of the confidence intervals of the diameter and polydispersity is the strong correlation between them. Therefore, the confidence interval would be smaller for larger sized parameters where the effects of the mean size and polydispersity on the scattering attenuation spectrum $\mu_s(k)$ can be better separated. The porosity obtained from the CDM is 12.5%, which is similar to reported in literature for silica particles grown with the Stöber method, where this varied between 9% and 13% [72–74].

The phase index of the suspended particles themselves is determined by means of comparing forward modeling with measurements. Therefore, we present here an unintrusive method to determine the refractive index of the colloidal particles within a suspension. This can be beneficial in the case of porous particles, where the phase index of the particles cannot be retrieved with an index matching experiment. Moreover, this provides an opportunity for particle sizing methods based on light scattering, since the CDM for the scattering attenuation is dependent on knowledge of the refractive index of the particles. In fact, uncertainty of the refractive index of the particle can be a limiting factor in the accuracy of particle sizing with Mie inversion [27,75]. Furthermore, the effective refractive index itself has been used for particle sizing for a few decades [35]. Therefore, understanding of the concentration dependence of the effective refractive index is important, at least to give an upper bound for the volume fraction under which the regularly used van de Hulst or Arago-Biot equations are valid.

In this work, the inversion required measurements at different *a priori* known volume fractions. Obviously, this is not possible when measuring at a single volume fraction. However, when the refractive index of the particle is known *a priori*, measurement of the group index could be used for direct measurement of the volume fraction [57]. This could eliminate the need for measurements at different volume fractions for determining the particle size.

Although, the wavelength range of 410 nm to 930 nm is broad, for distinguishing the effect of the mean diameter from the polydispersity, it is best to use a wavelength such that $x > 1$, i.e., using smaller wavelengths than used here for 100 nm particles. This will allow for a better PSD reconstruction due to the Mie resonances, even without parametrization of the PSD [76]. For the particles used in this work, this would mean measurements of fewer volume fractions would be required when the transmission would be measured at lower wavelengths.

## 6. CONCLUSION

In this work the concentration dependence of the effective complex refractive index of a colloidal suspension of 100 nm silica nanoparticles was investigated with spectral interferometry. For the real part of the effective refractive index, it was found that the group index scaled linearly with the volume fraction but that the concentration dependence of the GVD was nonlinear.

The data was compared to two models: the coupled dipole model proposed by Parola *et al.* provided both quantitatively and qualitatively a good description for both the group index and the GVD. The LF-QCA model did not predict the nonlinear behavior of the GVD.

The models were used in an iterative loop to estimate the mean particle radius, polydispersity, and porosity. For the CDM, the porosity of the particles was 12.5%. The particle size was found to be 102.2 nm with a polydispersity of 6.6%. The size distribution obtained with the small angle LF-QCA model had a mean diameter of 89.7 nm and a polydispersity of 19.8%. The results obtained with the CDM were in good agreement with electron microscopy measurements.

**Funding.** Nederlandse Organisatie voor Wetenschappelijk Onderzoek (P17-24, project 6).

**Acknowledgment.** We would like to thank Kelly J.H. Brouwer in collaboration with the Electron Microscopy Centre at Utrecht University for the TEM images she provided. We also would like to thank Ron Hoogerheide for technical support.

**Disclosures.** The authors declare no conflicts of interest.

**Data availability.** Data underlying the results presented in this paper and the relevant analysis routines are available in Ref. [77].

**Supplemental document.** See Supplement 1 for supporting content.

## REFERENCES

1. L. Lorenz, "Experimentale og theoretiske undersøgelser over legemernes brydningsforhold," Det K. Dan. Vidensk. Selsk. Skr. **5**, 483–518 (1875).
2. H. Lorentz, "Over het verband tusschen de voortplantingssnelheid van het licht en de dichtheid en samenstelling der middenstoffen," Verh. K. Acad. Wet. **18** (1879).
3. J. B. Biot and D. F. Arago, "Sur les affinités des corps pour la lumière, et particulièrement sur les forces réfringentes des différens gaz," Mém. Acad. Sci. Instit. France **6**, 301–387 (1806).
4. J. P. McClymer, "Precise determination of the refractive index of suspended particles: light transmission as a function of refractive index mismatch," Am. J. Phys **84**, 602–605 (2016).
5. J. C. M. Garnett, "XII. Colours in metal glasses and in metallic films," Philos. Trans. R. Soc. London A **203**, 385–420 (1904).
6. A. Parola, R. Piazza, and V. Degiorgio, "Optical extinction, refractive index, and multiple scattering for suspensions of interacting colloidal particles," J. Chem. Phys. **141**, 124902 (2014).
7. K. Ding and L. Tsang, "Effective propagation constants of dense nontenuous media with multi-species of particles," J. Electromagn. Waves Appl. **2**, 757–777 (1988).
8. D. A. G. Bruggeman, "Berechnung verschiedener physikalischer Konstanten von heterogenen Substanzen. I. Dielektrizitätskonstanten und Leitfähigkeiten der Mischkörper aus isotropen Substanzen," Ann. Phys. **416**, 636–664 (1935).
9. W. Heller, "The determination of refractive indices of colloidal particles by means of a new mixture rule or from measurements of light scattering," Phys. Rev. **68**, 5–10 (1945).
10. L. L. Foldy, "The multiple scattering of waves. I. General theory of isotropic scattering by randomly distributed scatterers," Phys. Rev. **67**, 107–119 (1945).

11. M. Lax, "Multiple scattering of waves," Rev. Mod. Phys. **23**, 287–310 (1951).
12. B. Zimm and W. Dandliker, *Theory of Light Scattering and Refractive Index of Solutions of Large Colloidal Particles* (American Chemical Society, 1954).
13. J. Keller, "Stochastic equations and wave propagation in random media," Proc. Symp. Appl. Math. **16**, 145–170 (1964).
14. H. Looyenga, "Dielectric constants of heterogeneous mixtures," Physica **31**, 401–406 (1965).
15. J. V. Champion, F. H. Meeten, and M. Senior, "Refraction by spherical colloid particles," J. Colloid Interface Sci. **72**, 471–482 (1979).
16. H. van de Hulst, *Light Scattering by Small Particles*, Dover Books on Physics (Dover, 1981).
17. L. Tsang, J. Kong, and R. Shin, *Theory of Microwave Remote Sensing*, Wiley Series in Remote Sensing and Image Processing (Wiley, 1985).
18. W. T. Doyle, "Optical properties of a suspension of metal spheres," Phys. Rev. B **39**, 9852–9858 (1989).
19. L. Hespel, S. Mainguy, and J. Greffet, "Theoretical and experimental investigation of the extinction in a dense distribution of particles: nonlocal effects," J. Opt. Soc. Am. A **18**, 3072–3076 (2001).
20. S. Durant, O. Calvo-Perez, N. Vukadinovic, *et al.*, "Light scattering by a random distribution of particles embedded in absorbing media: diagrammatic expansion of the extinction coefficient," J. Opt. Soc. Am. A **24**, 2943–2952 (2007).
21. Y. Battie, A. Resano-Garcia, N. Chaoui, *et al.*, "Extended Maxwell-Garnett-Mie formulation applied to size dispersion of metallic nanoparticles embedded in host liquid matrix," J. Chem. Phys. **140**, 044705 (2014).
22. A. Acevedo-Barrera and A. Garcia-Valenzuela, "Analytical approximation to the complex refractive index of nanofluids with extended applicability," Opt. Express **27**, 28048–28061 (2019).
23. A. Doicu and M. I. Mishchenko, "Electromagnetic scattering by discrete random media. I: The dispersion equation and the configuration-averaged exciting field," J. Quant. Spectrosc. Radiat. Transfer **230**, 282–303 (2019).
24. A. García-Valenzuela, A. Acevedo-Barrera, O. Vázquez-Estrada, *et al.*, "Full dynamic corrections to the Maxwell Garnett mixing formula and corresponding extensions beyond the dipolar approximation," J. Quant. Spectrosc. Radiat. Transfer **302**, 108578 (2023).
25. A. Nahmad-Rohen and A. García-Valenzuela, "Multiple-scattering model for the effective refractive index of dense suspensions of forward-scattering particles," J. Opt. Soc. Am. A **40**, 1552–1562 (2023).
26. A. Ishiniaru and Y. Kuga, "Attenuation constant of a coherent field in a dense distribution of particles," J. Opt. Soc. Am. **72**, 1317–1320 (1982).
27. V. D. Nguyen, D. J. Faber, E. van der Pol, *et al.*, "Dependent and multiple scattering in transmission and backscattering optical coherence tomography," Opt. Express **21**, 29145–29156 (2013).
28. B. Aernouts, R. Watté, R. V. Beers, *et al.*, "Flexible tool for simulating the bulk optical properties of polydisperse spherical particles in an absorbing host: experimental validation," Opt. Express **22**, 20223–20238 (2014).
29. M. Raju and S. Unni, "Concentration-dependent correlated scattering properties of intralipid 20% dilutions," Appl. Opt. **56**, 1157–1166 (2017).
30. G. Morales-Luna and A. García-Valenzuela, "Viability and fundamental limits of critical-angle refractometry of turbid colloids," Meas. Sci. Technol. **28**, 125203 (2017).
31. H. Contreras-Tello and A. García-Valenzuela, "Refractive index measurement of turbid media by transmission of backscattered light near the critical angle," Appl. Opt. **53**, 4768–4778 (2014).
32. F. Zernike and J. Prins, "Die Beugung von Röntgenstrahlen in Flüssigkeiten als Effekt der Molekülanordnung," Z. Phys. **41**, 184–194 (1927).
33. A. Vrij, "Mixtures of hard spheres in the Percus–Yevick approximation. Light scattering at finite angles," J. Chem. Phys. **71**, 3267–3270 (1979).
34. G. H. Meeten and A. N. North, "Refractive index measurement of turbid colloidal fluids by transmission near the critical angle," Meas. Sci. Technol. **2**, 441–447 (1991).
35. M. Mohammadi, "Colloidal refractometry: meaning and measurement of refractive index for dispersions; the science that time forgot," Adv. Colloid Interface Sci. **62**, 17–29 (1995).
36. A. Reyes-Coronado, A. García-Valenzuela, C. Sánchez-Pérez, *et al.*, "Measurement of the effective refractive index of a turbid colloidal suspension using light refraction," New J. Phys. **7**, 89 (2005).
37. C. Sánchez-Pérez, A. García-Valenzuela, R. Sato-Berrú, *et al.*, "Sizing colloidal particles from their contribution to the effective refractive index: experimental results," J. Phys. Conf. Ser. **274**, 012064 (2011).
38. R. Márquez-Islas and A. García-Valenzuela, "On the extinction coefficient of light in non-absorbing nanoparticle suspensions," Appl. Opt. **57**, 3390–3394 (2018).
39. F. Morales-Luna and A. García-Valenzuela, "Optical sizing of nanoparticles in thin films of nonabsorbing nanocolloids," Appl. Opt. **58**, 5989–5996 (2019).
40. T. Okubo, "Refractometric studies of "liquid-like" and "crystal-like" colloids in deionized solution," J. Colloid Interface Sci. **135**, 294–296 (1990).
41. G. H. Meeten, "Refractive index errors in the critical-angle and the Brewster-angle methods applied to absorbing and heterogeneous materials," Meas. Sci. Technol. **8**, 728–733 (1997).
42. E. Gutiérrez-Reyes, A. Garía-Valenzuela, and R. Barrera, "Extension of Fresnel's formulas for turbid colloidal suspensions: a rigorous treatment," J. Phys. Chem. B **118**, 6015–6031 (2014).
43. G. Morales-Luna, H. Contreras-Tello, A. García-Valenzuela, *et al.*, "Experimental test of reflectivity formulas for turbid colloids: beyond the Fresnel reflection amplitudes," J. Phys. Chem. B **120**, 583–595 (2016).
44. J. van der Horst, A. K. Trull, and J. Kalkman, "Deep-tissue label-free quantitative optical tomography," Optica **7**, 1682–1689 (2020).
45. A. K. Trull, J. van der Horst, J. G. Bijster, *et al.*, "Transmission optical coherence tomography based measurement of optical material properties," Opt. Express **23**, 33550–33563 (2015).
46. E. M. Purcell and C. R. Pennypacker, "Scattering and absorption of light by nonspherical dielectric grains," Astrophys. J. **186**, 705–714 (1973).
47. S. Edalatpour, M. čuma, T. Trueax, *et al.*, "Convergence analysis of the thermal discrete dipole approximation," Phys. Rev. E **91**, 063307 (2015).
48. F. Herz and S. Biehs, "Generalized coupled dipole method for thermal far-field radiation," Phys. Rev. B **105**, 205422 (2022).
49. R. G. Barrera and A. García-Valenzuela, "Coherent reflectance in a system of random Mie scatterers and its relation to the effective-medium approach," J. Opt. Soc. Am. A **20**, 296–311 (2003).
50. G. Mie, "Beiträge zur Optik trüber Medien, speziell kolloidaler Metallösungen," Ann. Phys. **330**, 377–445 (1908).
51. C. F. Bohren and D. R. Huffman, *Absorption and Scattering by a Sphere* (Wiley, 1998), Chap. 4, pp. 82–129.
52. M. Lax, "Multiple scattering of waves. II. The effective field in dense systems," Phys. Rev. **85**, 621–629 (1952).
53. M. Mishchenko, L. Travis, and A. Lacis, *Multiple Scattering of Light by Particles: Radiative Transfer and Coherent Backscattering* (Cambridge University, 2006).
54. J. K. Percus and G. J. Yevick, "Analysis of classical statistical mechanics by means of collective coordinates," Phys. Rev. **110**, 1–13 (1958).
55. J. Kong, L. Tsang, K. Ding, *et al.*, *Scattering of Electromagnetic Waves: Numerical Simulations*, Wiley Series in Remote Sensing (Wiley, 2001).
56. L. Tsang, J. A. Kong, and T. Habashy, "Multiple scattering of acoustic waves by random distribution of discrete spherical scatterers with the quasicrystalline and Percus–Yevick approximation," J. Acoust. Soc. Am. **71**, 552–558 (1982).
57. P. Speets and J. Kalkman, "Measuring optical properties of clear and turbid media with broadband spectral interferometry," Appl. Opt. **62**, 4349–4358 (2023).
58. G. Bradski, "The OpenCV Library," Dr. Dobb's J. Softw. Tools **25**, 120–123 (2000).

59. N. Otsu, "A threshold selection method from gray-level histograms," IEEE Trans. Syst. Man Cybern. **9**, 62–66 (1979).
60. M. Daimon and A. Masumura, "Measurement of the refractive index of distilled water from the near-infrared region to the ultraviolet region," Appl. Opt. **46**, 3811–3820 (2007).
61. I. H. Malitson, "Interspecimen comparison of the refractive index of fused silica*,†," J. Opt. Soc. Am. **55**, 1205–1209 (1965).
62. P. Virtanen, R. Gommers, T. E. Oliphant, *et al.*, "SciPy 1.0: fundamental algorithms for scientific computing in Python," Nat. Methods **17**, 261–272 (2020).
63. J. A. Nelder and R. Mead, "A simplex method for function minimization," Comput. J. **7**, 308–313 (1965).
64. E. Beale, "Confidence regions in non-linear estimation," J. R Stat. Soc. B **22**, 41–76 (1960).
65. K. W. Vugrin, L. P. Swiler, R. M. Roberts, *et al.*, "Confidence region estimation techniques for nonlinear regression in groundwater flow: three case studies," Water Resour. Res. **43**, W03423 (2007).
66. R. West, D. Gibbs, L. Tsang, *et al.*, "Comparison of optical scattering experiments and the quasi-crystalline approximation for dense media," J. Opt. Soc. Am. A **11**, 1854–1858 (1994).
67. A. García-Valenzuela, R. Márquez-Islas, and R. G. Barrera, "Reducing light-scattering losses in nanocolloids by increasing average inter-particle distance," Appl. Phys. A **123**, 84 (2017).
68. A. García-Valenzuela, H. Contreras-Tello, J. A. Olivares, *et al.*, "Insights into the dependent-scattering contributions to the extinction coefficient in highly scattering suspensions," J. Opt. Soc. Am. A **30**, 1328–1334 (2013).
69. P. Bertsch, A. Sánchez-Ferrer, M. Bagnani, *et al.*, "Ion-induced formation of nanocrystalline cellulose colloidal glasses containing nematic domains," Langmuir **35**, 4117–4124 (2019).
70. F. Dekker, B. Kuipers, Á. García, *et al.*, "Scattering from colloidal cubic silica shells: Part II, static structure factors and osmotic equation of state," J. Colloid Interface Sci. **571**, 267–274 (2020).
71. K. van Gruijthuijsen, M. Obiols-Rabasa, M. Heinen, *et al.*, "Sterically stabilized colloids with tunable repulsions," Langmuir **29**, 11199–11207 (2013).
72. G. Bogush, M. Tracy, and C. Zukoski, "Preparation of monodisperse silica particles: control of size and mass fraction," J. Non-Cryst. Solids **104**, 95–106 (1988).
73. S. R. Parnell, A. L. Washington, A. J. Parnell, *et al.*, "Porosity of silica Stöber particles determined by spin-echo small angle neutron scattering," Soft Matter **12**, 4709–4714 (2016).
74. Y. Zheng, L. Zhou, Y. Dong, *et al.*, "Robust optical-levitation-based metrology of nanoparticle's position and mass," Phys. Rev. Lett. **124**, 223603 (2020).
75. P. Eneren, Y. Aksoy, Y. Zhu, *et al.*, "Light extinction spectroscopy applied to polystyrene colloids: sensitivity to complex refractive index uncertainties and to noise," J. Quant. Spectrosc. Radiat. Transfer **261**, 107494 (2021).
76. F. Ferri, A. Bassini, and E. Paganini, "Modified version of the Chahine algorithm to invert spectral extinction data for particle sizing," Appl. Opt. **34**, 5829–5839 (1995).
77. P. N. A. Speets and J. Kalkman, "Experiment and theory of the complex refractive index of dense colloidal media—data and analysis," Zenodo, 2023, https://doi.org/10.5281/zenodo.10247006.